7-23-2014

Electron-Ion Equilibrium and Shock Precursors in the Northeast Limb of the Cygnus Loop

Amber A. Medina
Harvard-Smithsonian Center for Astrophysics

John C. Raymond
Harvard-Smithsonian Center for Astrophysics

Richard J. Edgar
Harvard-Smithsonian Center for Astrophysics

Nelson Caldwell
Harvard-Smithsonian Center for Astrophysics

Robert A. Fesen
Dartmouth College

See next page for additional authors

The Astrophysical Journal, 791:30 (11pp), 2014 August 10 doi:10.1088/0004-637X/791/1/30

ELECTRON–ION EQUILIBRIUM AND SHOCK PRECURSORS IN THE NORTHEAST LIMB OF THE CYGNUS LOOP

Amber A. Medina[1,2], John C. Raymond[1], Richard J. Edgar[1], Nelson Caldwell[1], Robert A. Fesen[3], and Dan Milisavljevic[1]
[1] Harvard-Smithsonian Center for Astrophysics, 60 Garden Street, Cambridge, MA 02138, USA; amedina@cfa.harvard.edu, jraymond@cfa.harvard.edu, edgar@head.cfa.harvard.edu
[2] Department of Physics, New Mexico State University, 1255 N Horseshoe, Las Cruces, NM 88003-88001, USA; amedina7@nmsu.edu
[3] Department of Physics and Astronomy, Dartmouth College, 6127 Wilder Lab, Hanover, NH 03755, USA
Received 2014 January 13; accepted 2014 June 12; published 2014 July 23

ABSTRACT

We present an observational study using high-resolution echelle spectroscopy of collisionless shocks in the Cygnus Loop supernova remnant. Measured Hα line profiles constrain pre-shock heating processes, shock speeds, and electron–ion equilibration (T_e/T_i). The shocks produce faint Hα emission line profiles, which are characterized by narrow and broad components. The narrow component is representative of the pre-shock conditions, while the broad component is produced after charge transfer between neutrals entering the shock and protons in the post-shock gas, thus reflecting the properties of the post-shock gas. We observe a diffuse Hα region extending about 2.′5 ahead of the shock with line width $\sim$29 km s^{-1}, while the Hα profile of the shock itself consists of broader than expected narrow (36 km s^{-1}) and broad (250 km s^{-1}) components. The observed diffuse emission arises in a photoionization precursor heated to about 18,000 K by He I and He II emission from the shock, with additional narrow component broadening originating from a thin cosmic-ray precursor. Broad to narrow component intensity ratios of $\sim$1.0 imply full electron–ion temperature equilibration $T_e \simeq T_i$ in the post-shock region. Broad component line widths indicate shock velocities of about 400 km s^{-1}. Combining the shock velocities with proper motions suggests that the distance to the Cygnus Loop is $\sim$890 pc, significantly greater than the generally accepted upper limit of 637 pc.

Key words: acceleration of particles – ISM: individual objects (Cygnus Loop) – ISM: supernova remnants – shock waves

Online-only material: color figures

1. INTRODUCTION

Supernovae are energetic phenomena ($\sim 10^{51}$ erg). They produce supersonic ejecta that travel at velocities up to $\sim$30,000 km s^{-1} driving shock waves into the interstellar medium (ISM; Chevalier & Gardner 1974). Measurements of pre-shock heating and post-shock temperatures make it possible to study the physics of collisionless supernova remnant (SNR) shocks. Special diagnostics arise if the pre-shock plasma is partially neutral. The partially neutral hydrogen produces Hα emission with a line profile that indicates electron and proton temperatures. The line profile also provides a laboratory for interstellar cosmic-ray acceleration, because it is sensitive to the precursor where cosmic-rays are accelerated, and the thickness of the precursor depends on the cosmic-ray diffusion coefficient, κ (Blandford & Eichler 1987). Analysis of the Hα emission produced in collisionless non-radiative shocks can set limits on κ, provide shock speeds (and if proper motions are available, SNR distances), and act as a probe for electron–ion thermal equilibration ($T_e \simeq T_i$) in astrophysical shocks.

The Cygnus Loop is a well-suited SNR for enhancing our understanding of shock wave physics (Treffers 1981; Raymond et al. 1983; Hester et al. 1994; Ghavamian et al. 2001). The Loop is a frequently studied middle-aged SNR $\sim$ 10,000 yr old, believed to be the result of a cavity explosion (Levenson et al. 1997, 1998). Due to its size ($d = 3^\circ$), proximity (<1 kpc), and surface brightness, structures in the remnant are resolvable at optical and X-ray wavelengths, and they are observable in the UV due to low reddening (Blair et al. 2009). The Loop contains both non-radiative and radiative shocks in the northeast and southeastern regions, respectively (see Figure 1). The presence of both types of shocks plus photoionization precursors (Ballet et al. 1984; Szentgyorgyi et al. 2000) provides an ideal site for the study of SNR physics. Balmer-dominated filaments in its northeast limb, in particular, provide a laboratory for disentangling the microphysics (pre-heating, T_e/T_i equilibrium, and comic-ray acceleration) of shock waves generated in SNRs (Raymond et al. 1980; Long et al. 1992). Sections 2 and 3 present background information on Balmer-dominated shocks and on different types of shock precursors. We then discuss the observations and analysis of the results. We conclude that the distance to the Cygnus Loop is likely to be larger than previously thought, the effective electron–ion thermal equilibration occurs in the shocks studied, and that heating in a photoionization precursor accounts for about half elevated pre-shock temperature inferred from the Hα profiles. We obtain an upper limit to the cosmic ray diffusion coefficient intermediate between other estimates.

2. BALMER-DOMINATED FILAMENTS

In the outer edges of several SNRs, warm ($T \sim 10^4$ K) unshocked gas is hit by non-radiative collisionless shocks. Non-radiative shocks are able to preserve the shock signatures because the Coulomb collision timescale is greater than the age of the shock (McKee & Hollenbach 1980). Lack of collisions implies different particle species do not reach thermal equilibrium, so that electron temperature, T_e, does not necessarily equal ion temperature, T_i. While the Hα emission from a non-radiative shock arises immediately behind the shock, most of

Table 1
Previously Measured Hα Narrow and Broad Components

Paper	Position		Exposure Time	$FWHM_N$	$FWHM_B$
	α_{J2000}	δ_{J2000}	(s)	(km s^{-1})	(km s^{-1})
Treffers (1981)	20 43 11.00	30 51 20.0	14,400	∼35	$\geqslant 130$
Raymond et al. (1983)	20 53 58.96	31 45 6.00	37,000	31 ± 8	167 ± 42
Hester et al. (1994)	20 53 58.96	31 45 6.00	3,000	∼33	∼130
Ghavamian et al. (2001)	20 54 32.50	32 17 32.8	5,400	-	262 ± 32

Note. - Unable to resolve narrow component.

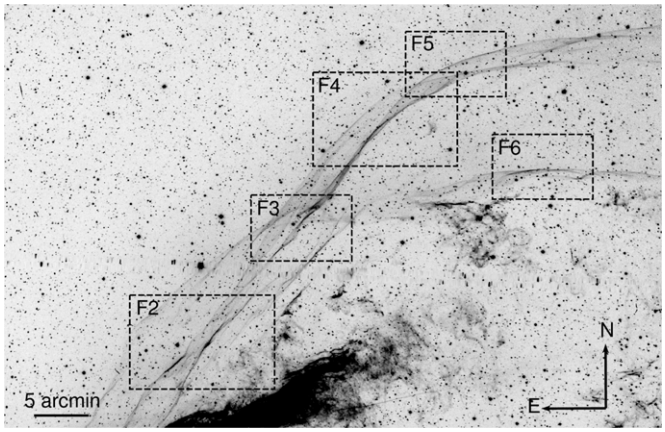

Figure 1. Optical image in Hα of the supernova remnant, the Cygnus Loop obtained at the Burrell Schmidt telescope located at Kitt Peak National Observatory. Acquired in 1993 with an exposure time of 1500 s. Non-radiative shocks can be seen as faint filaments in the northeast region, while the darker region in the southeast indicates the presence of a radiative shock. Dashed rectangular boxes indicate zoomed in regions analyzed in this study displayed in Figures 2–6.

the optical emission from radiative shock waves is produced far downstream, long after Coulomb collisions have brought the particle species into thermal equilibrium. Non-radiative collisionless shock waves ranging from 350 to 450 km s^{-1} produce faint filaments dominated by Balmer line emission in the northeastern region of the Cygnus Loop, and much faster shocks are seen in younger SNRs. Pre- and post-shock speeds, pre-shock heating mechanisms, and post-shock equilibration processes can be obtained through detailed analysis of these non-radiative collisionless shocks.

When a non-radiative shock encounters neutral hydrogen atoms, faint line emission is produced by excitation of H atoms before ionization can occur. As cold hydrogen atoms enter post-shock gas, they have a 30% probability of being excited to the $n = 3$ level, producing Lyman and Balmer lines directly behind the shock front. Two-thirds of the emission produced is Hα, leading to a net 0.2 Hα photons per neutral hydrogen atom entering the shock (Raymond 1991). The resulting Balmer-dominated filamentary structures outline the X-ray emission of the SNR (Raymond 1991; Heng 2010).

The Hα profiles of Balmer-dominated filaments contain a narrow (∼10–40 km s^{-1}) Hα component from cold neutral hydrogen atoms excited by electrons in the post-shock region. Thus, the width of the narrow component corresponds to the pre-shock temperature. However, some atoms undergo charge transfer with protons in the post-shock gas before being excited, and they produce a broad (∼150–2000 km s^{-1} for 200–3000 km s^{-1} shocks) component of Hα. The width of the broad component corresponds to the proton kinetic temperature of the post-shock region, T_i (Chevalier & Raymond 1978; Chevalier et al. 1980; Smith et al. 1994; Ghavamian et al. 2002). The ratio of the broad to narrow component intensities, I_b/I_n, is a function of the relative rates of charge transfer and ionization behind the shock. The value of I_b/I_n determines electron–ion temperature equilibration because it is sensitive to T_e.

3. SHOCK PRECURSOR

Previous measurements of narrow component Hα line widths in SNRs indicate pre-shock temperatures ∼28,000 to 50,000 K (Hester et al. 1994; Smith et al. 1994; Ghavamian et al. 2001). However, temperatures $T \geqslant 15{,}000$ K lead to complete ionization of neutral hydrogen in equilibrium, so that Hα emission from the filament would not be detected. Thus the observation of Hα emission implies that the pre-shock gas is heated in a thin precursor.

Several types of precursor are possible, but some can be excluded. A thermal conduction precursor (Zel'dovich & Raizer 1966) heats the electrons and ionizes the gas before it reaches the shock, so no broad component would be seen (Smith et al. 1994). An MHD precursor (Mullan 1971; Draine 1980; Graham et al. 1991; Curiel 1992) would require a shock speed below the Alfvén speed, while the Alfvén speed ahead of the Cygnus Loop shock is only around 20 km s^{-1} for typical ISM magnetic field strengths. A precursor can also be produced by broad component neutrals leaking back through the shock and depositing energy upstream (Hester et al. 1994; Smith et al. 1994; Morlino et al. 2012), but the small pre-shock neutral fraction in the NE Cygnus Loop (Ghavamian et al. 2001) implies that this process is ineffective (Nikolić et al. 2013).

We are left with two types of precursor to consider; a cosmic-ray precursor and a photoionization precursor.

3.1. Cosmic-ray Precursor

A precursor where particles scatter off plasma turbulence is an integral part of the diffusive shock acceleration model for cosmic-ray acceleration (Blandford & Eichler 1987). The turbulence directly produces bulk motions, and it heats the pre-shock gas as the turbulence dissipates, broadening the width of the Hα narrow component (Raymond et al. 2011; Ohira 2012). Cosmic-ray precursors in SNR have been inferred spectroscopically from unexpectedly broad narrow components (see Table 1). Smith et al. (1994), Ghavamian et al. (2002), and Sollerman et al. (2003) measured narrow component widths in various SNR (the Cygnus Loop, RCW 86, Tycho, SN1006, and Kepler) ranging from 30 to 50 km s^{-1} corresponding to pre-shock temperatures of 20,000–50,000 K. Lee et al. (2007, 2010) spatially resolved the precursor in Tycho's SNR by observing

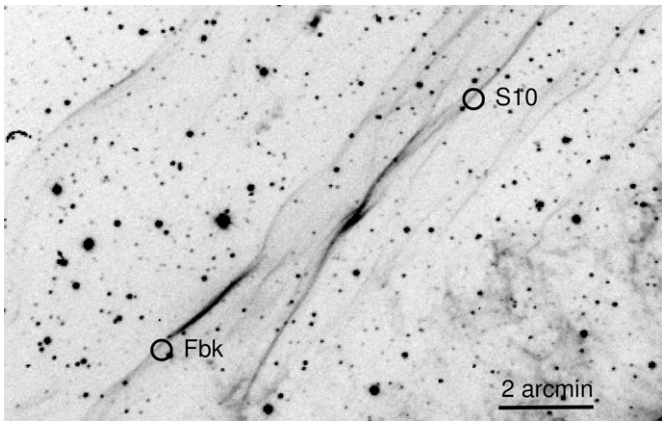

Figure 2. Southernmost positions on Loop showing groups Fbk and S10.

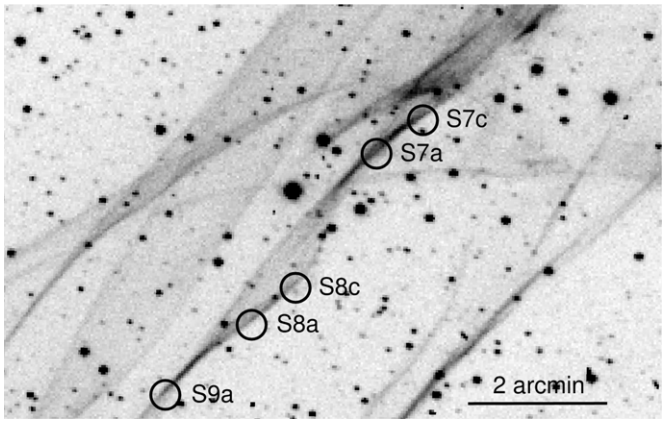

Figure 3. Lower region of the filament showing fiber groupings S89 and S7.

emission ahead of the shock in a $\sim 1''$ region interpreted as the precursor with line widths of $\sim$45 km s^{-1} corresponding to a pre-shock temperature of $\sim$45,000 K. Evidence for particle acceleration in SNR originates from observations of radio and X-ray synchrotron emission (Reynolds & Ellison 1992; Vink et al. 2006; Allen et al. 2008). Cosmic-ray acceleration is sensitive to the thickness d of the precursor, which, for Balmer-dominated filaments, is constrained by the requirement that the incoming neutral hydrogen must not be completely ionized before reaching the shock front (Boulares & Cox 1988). The thickness can be inferred from the shock velocity v_s and the diffusion coefficient κ previously mentioned in Section 1, where $d \simeq \kappa / v_s$. Thus, κ can be constrained by probing the properties of the precursor contained in the narrow component Hα emission and the faint diffuse Hα region extending ahead of the filament (Hester et al. 1994; Lee et al. 2007, 2010). κ has been estimated $\sim 2 \times 10^{24}$ cm s^{-1} by Hester et al. (1994) while Li & Chen (2012), using models of *Fermi* Large Area Telescope (LAT) gamma ray emission from the Cygnus Loop, estimated $\sim 4 \times 10^{26}$. This wide range indicates that κ needs to be further constrained in order to quantify the ability of SNR shock waves to accelerate cosmic-rays.

A recent study (Salvesen et al. 2009) attempted to confront cosmic-ray acceleration theory in the Cygnus Loop by examining cosmic-ray to gas pressure ratios P_{CR}/P_G. They found upper limits that are formally negative for the ratios P_{CR}/P_G at some positions due to uncertainties in distance, post-shock temperatures, and electron–ion equilibration. Salvesen's results are thus are inconclusive about cosmic-ray acceleration in the Loop.

3.2. Photoionization Precursor

Photoionization precursors have been observed ahead of radiative shocks in the eastern region of the Cygnus Loop, where the shocked gas can be spatially separated from the photoionization precursor (Ballet et al. 1984; Szentgyorgyi et al. 2000). The precursor appears as a faint diffuse region ahead of the shock filament similar to the steady-state models of Shull & McKee (1979) and Dopita & Sutherland (1996). The photoionization precursors of non-radiative shocks are somewhat different in that the ionizing radiation is mostly made up of He I and He II photons (Ghavamian et al. 2000). Non-radiative shocks in Balmer-dominated regions produce roughly 0.4 ionizing He I 584 Å and He II 304 Å photons per hydrogen atom at energies of 21.2 eV and 40.8 eV, respectively. As neutral hydrogen absorbs helium photons, it produces strong electron heating. The signatures of the photoionization precursor are enhanced Hα emission, increased temperature, and increased [N II] emission over a region whose thickness is on the order of the mean-free path of the photons, which is $\sim 10^{18}$ cm for He I and $\sim 10^{19}$ cm for He II.

4. OBSERVATIONS AND DATA REDUCTION

Using the multiobject optical echelle spectrograph HECTOCHELLE, located at the MMT 6.5 m telescope on Mount Hopkins, Arizona (Szentgyorgyi et al. 2011), we observed 240 locations spanning 1° along the NE limb of the Cygnus Loop. The positions on the filament were selected based on previous measurements of the Balmer-dominated NE region of the Loop (Raymond et al. 1983, 2013; Hester et al. 1994; Ghavamian et al. 2001; Salvesen et al. 2009). The 1.″5 diameter optical fibers probed not only the filament, but also the dark sky and diffuse Hα emission surrounding the region. Although HECTOCHELLE is capable of fiber placement as close as 25″ apart, the requirement that fibers cannot cross meant we sampled positions at roughly twice that separation. We were able to obtain Hα emission line profiles at the proposed primary positions and at positions displaced 1.″5 northeast of each primary fiber. The offset between what we refer to as ON and OFF positions was made to search for variations across the filament and to check for positional errors due to the proper motion correction, which is based on Salvesen et al. (2009). We later found, however, that the World Coordinate System of the image used for choosing positions (Figure 1) had a systematic offset in the southern part of the image. The worst deviation is seen in Figure 2, where the fiber was placed nearly 10″ behind the brightest part of the filament.

With a resolution of $R \sim 38{,}000$, HECTOCHELLE is capable of resolving the line profiles from the Balmer-dominated filaments in the Cygnus Loop. With the OB 25 filter, the Hα emission line at 6563 Å, as well as [N II] at 6548 Å and 6584 Å were observed. Our data were taken at two different times approximately two hours apart on 2012 October 13. Both data sets were exposed for 90 minutes, broken into subexposures for cosmic ray rejection. The data were reduced using standard IRAF[4] procedures. The raw images were processed, and the individual spectra were wavelength calibrated in the standard way.

[4] IRAF is distributed by the National Optical Astronomy Observatories, which are operated by the Association of Universities for Research in Astronomy, Inc., under cooperative agreement with the National Science Foundation.

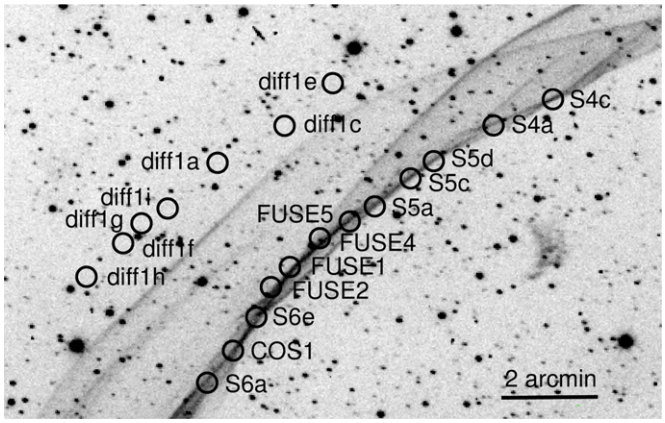

Figure 4. Middle region of the filament showing diffuse Hα denoted by the prefix "diff" and fiber groupings COS1, S(4, 5, 6), FUSEA, and FUSEB.

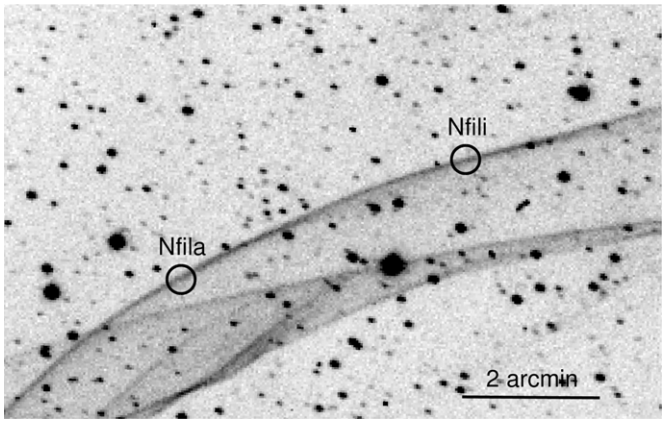

Figure 5. Northern region of the filament showing fiber group North Filament (NFil).

Table 2
Fiber Positions

Filament Name	α_{J2000} (h, m, s)	δ_{J2000} (○, m, s)
Fbk	20 56 08.113	31 55 41
S10	20 55 37.015	32 01 02
S9a	20 55 20.755	32 06 33
S8a	20 55 14.912	32 07 33
S7a	20 55 06.438	32 10 01
S7c	20 55 03.294	32 10 30
S6a	20 54 46.203	32 15 23
COS 1	20 54 43.614	32 16 04
S6e	20 54 41.273	32 16 46
FUSE2	20 54 39.810	32 17 25
FUSE1	20 54 37.901	32 17 50
FUSE4	20 54 34.901	32 18 27
FUSE5	20 54 31.900	32 18 48
S5a	20 54 17.474	32 20 51
S5c	20 54 25.803	32 19 43
S5d	20 54 23.475	32 20 05
S4a	20 54 17.474	32 20 51
S4c	20 54 11.514	32 21 24
NFila	20 54 12.180	32 23 02
NFili	20 53 52.336	32 24 48
EWfila	20 53 23.373	32 14 20
EWfild	20:53:28.337	32 14 18

Notes. Coordinates listed for the measured positions along the filament.

4.1. Region Selection

The majority of our positions along the non-radiative shock filaments corresponded to previous UV or optical observations. The positions denoted S4 through S10 correspond to filament segments whose proper motions were measured by Salvesen et al. (2009), with the appended letter indicating a position along that segment. COS1 corresponds to the UV spectrum obtained by the Cosmic Origins Spectrograph (COS) on the *Hubble Space Telescope* (*HST*; Raymond et al. 2013). FUSE1 through FUSE5 lie on a filament whose UV spectrum was obtained with the *FUSE* satellite and indicates approximate oxygen-proton thermal equilibration Raymond et al. (2003). Position Fbk lies near a filament studied by Fesen et al. (1982), Raymond et al. (1983), Long et al. (1992), Hester et al. (1994), Sankrit et al. (2000), Sankrit & Blair (2002) and Blair et al. (2005). Note that the Fbk HECTOCHELLE position lies near one end of the filament, while the other observations were centered near the middle. Ghavamian et al. (2001) obtained a lower resolution Hα line profile at a position in between segments S5 and S6. We also observed some positions that have not been previously observed. EWfil and Nfil were selected from the Hα image as bright, distinct filaments whose profiles could be compared with those of the other targets.

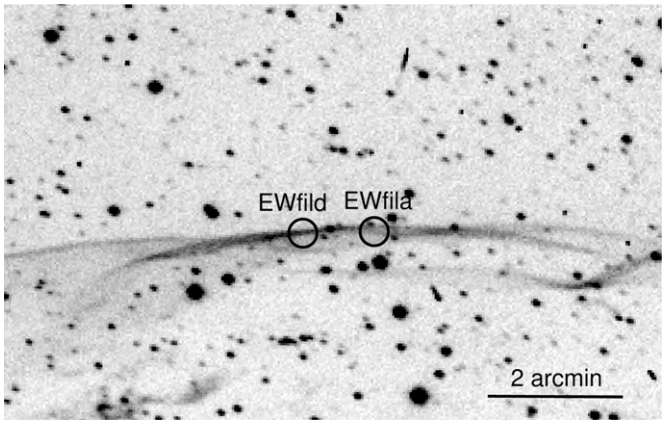

Figure 6. Filament lying perpendicular to main filament showing fiber group EWfil.

We grouped nearby fiber positions with similar characteristics in order to increase the signal-to-noise ratio (S/N). The groups of spectra had spectral features occurring at velocities within 2–3 km s^{-1} of each other and were located within close proximity on the filament, thus leading to similar intensities, centroids, and line widths of both Hα and [N II]. The 12 groupings of fibers were chosen (Table 2 and Figures 2–6) along with 7 diffuse positions and 7 positions from the surrounding dark sky. Right ascension and declination of all the filament fiber positions can be seen in Table 2, but for completeness it is important to note which fiber spectra have been added together. FUSEA is the summation of FUSE1 and FUSE2. FUSEB is the summation of FUSE4 and FUSE5. S4 is the summation of S4a and S4c. S5 sums S5a, S5c, and S5d. S6 sums positions S6a and S6e. Note that although COS1 lies in between S6a and S6e (Figure 4), we did not include COS1 in the sum so that the COS1 Hα profiles could be used with the UV spectrum from COS (Figure 8; Raymond et al. 2013). S7 is the summation of S7a and S7c. S89 is the summation of S8a and S9a. Nfil sums Nfila and Nfili and lastly, EWfil is the summation of EWfila and EWfild.

Table 3
Sky and Diffuse Hα and [N II] Emission

	FWHM$_1$ (km s^{-1})	FWHM$_2$ (km s^{-1})	I_1 [10^{-5}] (photon cm^{-2} s^{-1} arcsec^{-2})	I_2 [10^{-5}] (photon cm^{-2} s^{-1} arcsec^{-2})	Centroid$_1$ (km s^{-1})	Centroid$_2$ (km s^{-1})
Sky$_{ON}$ Hα	12 ± 0.41	38 ± 2.4	1.56 ± 0.47	2.02 ± 0.61	−3.2 ± 0.14	5.4 ± 1.2
Sky$_{ON}$ [N II]	...	...	1.08 ± 0.32	0.63 ± 0.19	8.2 ± 0.50	49 ± 0.87
Sky$_{OFF}$ Hα	13 ± 0.34	63 ± 2.8	1.50 ± 0.45	2.33 ± 0.70	−2.3 ± 0.12	13 ± 1.2
Sky$_{OFF}$ [N II]	...	...	0.88 ± 0.14	0.167 ± 0.05	9 ± 0.73	48 ± 0.92
Diffuse$_{ON}$ Hα	31 ± 0.7	26 ± 1.1	19.6 ± 5.9	8.0 ± 2.4	8.2 ± 0.3	49 ± 0.5
Diffuse$_{ON}$ [N II]	...	...	1.77 ± 0.53	1.57 ± 0.47	...	...
Diffuse$_{OFF}$ Hα	29 ± 0.5	23 ± 1.7	20.1 ± 6.0	3.12 ± 0.9	7.6 ± 0.2	53 ± 1.7
Diffuse $_{OFF}$ [N II]	...	...	2.87 ± 0.8	2.17 ± 0.7	...	...

Notes. Line widths, intensities, and centroids for emission from two components of Hα and two components of [N II] (1,2) present in the sky and diffuse background. The centroids of Hα and [N II] are both determined relative to their respective rest wavelengths. Line widths for [N II] are not reported due to low signal to noise. The diffuse [N II] velocity centroids are linked to the Hα emission centroids and thus are not reported.

Table 4
Hα Line Widths, Intensities, and Centroids for ON Fiber Positions

	FWHM$_B$ (km s^{-1})	Centroid$_B$ (km s^{-1})	FWHM$_N$ (km s^{-1})	Centroid$_N$ (km s^{-1})	I_b/I_n	I_B (10^{-5} photons cm^{-2} s^{-1}arcsec^{-2})
			Position			
EWfil	209 ± 7.0	−6.7 ± 0.5	38 ± 0.7	5.4 ± 0.2	0.883 ± 0.05	15.6 ± 4.7
Nfil	298 ± 40	−23 ± 6.0	36 ± 0.8	7.6 ± 0.3	0.649 ± 0.10	10.4 ± 3. 1
S4	219 ± 13	6.9 ± 3.2	43 ± 2.0	9.8 ± 0.6	1.39 ± 0.15	10.9 ± 3.3
S5	203 ± 7.0	6.5 ± 1.8	40 ± 0.8	7.7 ± 0.3	1.09 ± 0.06	21.4 ± 6.4
FUSEA	296 ± 13	−16 ± 3.3	36 ± 0.5	6.1 ± 0.2	0.761 ± 0.04	14.3 ± 4.3
FUSEB	270 ± 9.8	7.1 ± 2.7	36 ± 0.6	7.1 ± 0.2	0.942 ± 0.05	16.7 ± 5.0
COS1	255 ± 15	16 ± 4.0	39 ± 1.0	6.2 ± 0.5	1.16 ± 0.11	10.6 ± 3.2
S6	239 ± 6.0	13 ± 1.6	38 ± 0.5	6.9 ± 0.2	0.962 ± 0.04	22.3 ± 6.7
S7	178 ± 8.0	26 ± 3.0	35 ± 0.9	5.4 ± 0.4	0.831 ± 0.07	10.2 ± 3.1
S89	347 ± 39	1.0 ± 7.8	37 ± 1.1	4.1 ± 0.4	0.874 ± 0.12	7.14 ± 2.1
S10	141 ± 83	−59 ± 29	35 ± 3.5	3.4 ± 1.8	0.342 ± 0.31	1.18 ± 0.35
Fbk	290 ± 38	23 ± 11	35 ± 1.2	7.2 ± 0.5	0.597 ± 0.12	4.32 ± 1.3

Notes. Line widths, centroids, broad to narrow intensity ratios and broad component intensity for the ON fibers chosen along the filament. Parameters where determined by fits described previously.

4.2. Profile Fitting

Fitting the narrow and broad components of Hα was accomplished using Sherpa coupled with CIAO 4.5 modeling and fitting procedures (Doe et al. 2007; Freeman et al. 2001; Fruscione et al. 2006). To construct a background for subtraction, seven fiber spectra from dark sky regions 10′ to 15′ NW from the filament around $\alpha_{J2000} \simeq 20^h56^m04^s$ and $\delta_{J2000} \simeq 32°24'17''$ were averaged, as well as the seven diffuse fiber positions shown in Figure 4 around $\alpha_{J2000} \simeq 20^h54^m45^s$ and $\delta_{J2000} \simeq 32°20'03''$ chosen to sample the photoionization precursor. The sky was fit with a polynomial background to account for the continuum, while Gaussians were used to represent Geocoronal and Galactic background Hα emission lines, the two [N II] lines, and two narrow night sky lines at ≃270 and ≃670 km s^{-1}. The $R \sim 38{,}000$ resolution is confirmed by the line widths of the night sky lines. Table 3 shows little difference between the ON and OFF sky spectra except for the unexpectedly large difference in the widths of one of the Hα components. This probably indicates some degeneracy in the fitting of overlapping components. The night sky lines also changed somewhat as the night progressed. The [N II] lines also showed a component of Galactic background emission near +48 km s^{-1}.

As a check, we compared our sky spectra with the Hα emission from the Wisconsin H-Alpha Mapper (WHAM). WHAM produced a sensitive high spectral resolution survey of the Milky Way in Hα with about 1 degree spatial resolution (Haffner et al. 2003). The positions to the NE of the Cygnus Loop showed intensities of about 1.0 × 10^{-5} ph cm^{-2} s^{-1} arcsec^{-2} at LSR velocities of about 1 to 10 km s^{-1}. Some of the nearby WHAM positions also showed components at about +45 km s^{-1}, which agrees with the centroids of the red components of the [N II] lines after a correction of 2.6 km s^{-1} from LSR to the observed velocity. The Hα intensities quoted in Tables 3 and 4 are based on a comparison of the number of photons detected in the COS1 spectrum with the Hα intensity given by Raymond et al. (2013). The calibration is uncertain by about 30% because of variation in the transmission of individual fibers and the placement of our fiber within diameter of the 2.″5 COS aperture. Overall, our sky background (Table 3) agrees well with the WHAM observations. When we use the sky and diffuse spectra as backgrounds in fitting the filament spectra, the intensity normalization is a free parameter in order to account for the variations in transmission among different fibers.

Diffuse Hα emission is observed at various positions ahead of the filament. We fit the sum of the spectra at the seven positions

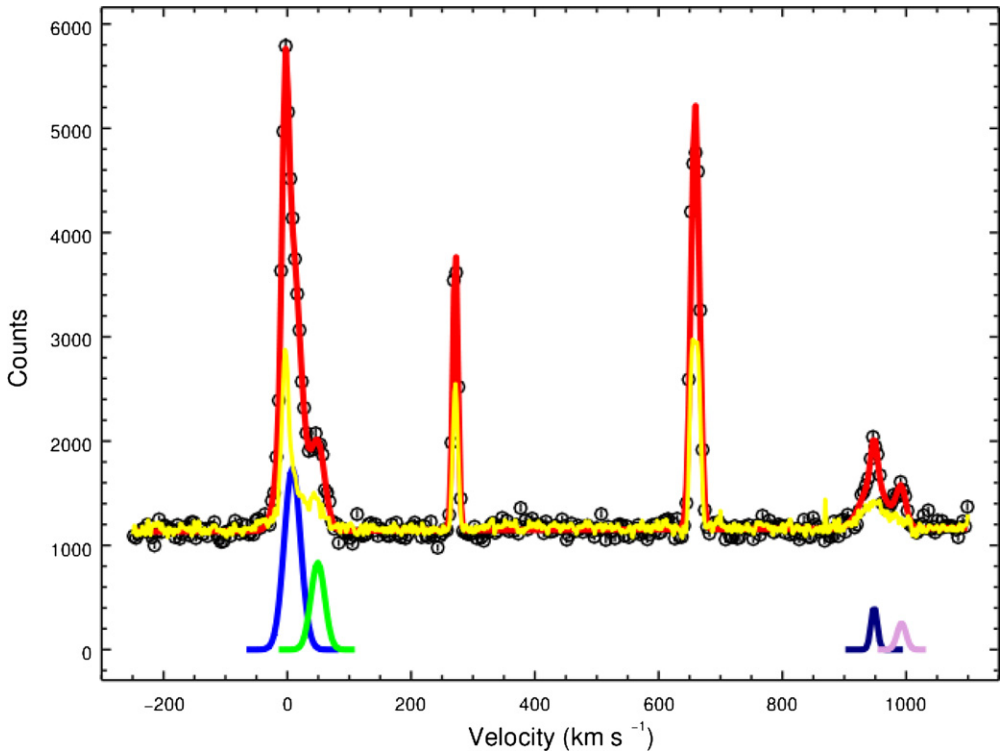

Figure 7. Fit to the diffuse Hα region ahead of the filament, using the sky as a background. The plot shows the model fit to the data points (red), separated Hα emission components from the diffuse precursor (blue) and Galactic contribution (green). Also shown is the separation of the [N II] emission components (navy) and (purple). Shown in yellow is the raw sky spectrum used as a background.

(A color version of this figure is available in the online journal.)

labeled diff in Figure 4 with a sky spectrum plus two Gaussians for Hα (background Hα and precursor) and the [N II] lines separately for the ON and OFF spectra. As shown in Table 3, there is fairly strong emission at about +50 km s^{-1}, which we attribute to the strongly varying galactic background. The component near 8 km s^{-1} seen in in the average diffuse spectrum is the one associated with the Cygnus Loop. The scaling factors for the ON and OFF spectra were fitted separately. The resulting Hα and [N II] parameters (Table 3) are used for the analysis of the photoionization precursor.

The diffuse spectrum is also used as the background contribution for the emission at the filament positions (sky + diffuse Hα + [N II] with scaling factor). The diffuse positions chosen had good S/N, and they are typical of the diffuse positions we observed. In this case, the background scaling factor must account not only for variations in fiber sensitivity but also for variations in the diffuse emission intensity in the region. In particular, the diffuse background can change across the filament where the photoionized gas is suddenly heated to X-ray emitting temperatures. The fits to the filament profiles assume a double Gaussian for Hα (broad and narrow components) plus background. Thus, the fits will choose a background scaling factor that minimizes the continuum, night sky and [N II] residuals. Nevertheless, the uncertainty in the background Hα probably dominates the uncertainty in the broad-to-narrow intensity ratio I_b/I_n. Example fits to the filament spectra are seen in Figures 8–11 for the COS1, Nfil ON and OFF, and FUSEA positions. A typical fit is performed on ∼400 data points with eight free parameters.

5. ANALYSIS

Our analysis of optical echelle spectra of Balmer-dominated filaments in the northeastern Cygnus Loop indicates the presence of a shock precursor and provides us with accurate information needed to determine shock velocities and pre- and post-shock temperatures. From these, we can infer electron–ion temperature ratios determined from broad to narrow Hα intensity ratios I_b/I_n. We can also constrain the cosmic-ray diffusion coefficient, κ, and combine the shock speeds with proper motion measurements to obtain the distance to the Cygnus Loop. The results are discussed in the following sections.

5.1. Precursor

Line widths, centroids, and intensities of the diffuse Hα emission were measured in order to determine the pre-heating mechanism in the Cygnus Loop discussed in Section 3. The S/N for [N II] is low in the diffuse spectra, so we report only the intensities for the relevant components (Table 3). Hα emission lies ahead of the shock filament and extends into the ISM ∼2.′5 in a diffuse region around $\alpha_{J2000} \simeq 20^h54^m45^s$ and $\delta_{J2000} \simeq 32°20'03''$. The diffuse emission is clearly visible in deep Hα images, though it is not obvious in Figure 1, for which we chose a stretch that emphasizes the structure of the filaments. Figures 1–4 also show faint filaments ahead of the bright filaments we study. The emission from the filaments and the faint regions between the filaments arises from a rippled shock front seen nearly edge-on (Hester 1987). Although diffuse emission can be seen at various regions along the filament, we chose to explore the emission lying ahead of the bulk of our fiber positions along the filament (Figure 4). Seven diffuse fiber spectra were averaged to increase the S/N. Two Gaussians were used to fit the Hα emission (Figure 7). One Gaussian measured the direct Hα emission coming from the diffuse region while the other is red shifted to ∼50 km s^{-1} in both the ON and OFF spectra. As discussed above, we interpret the additional

red-shifted emission as a component of the Galactic Hα emission that varies strongly across the field.

The width of the Hα line profile is 29 ± 0.52 km s^{-1} in the OFF and 31 ± 0.68 km s^{-1} in the ON spectra. Correction for the instrumental resolution of 9.0 km s^{-1} gives the average line width of 28.6 km s^{-1} corresponding to the precursor gas temperature ∼18,000 K. Also present in the diffuse region is faint [N II] at 6584 Å. The intensity ratios of [N II]/Hα in the ON and OFF spectra are 0.11 ± 0.01 and 0.08 ± 0.01, respectively. The ratios indicate a gas having a temperature far upstream of ∼6000 K. Ionization of neutral hydrogen by He I and He II photons as the gas propagates toward the shock front is a possible explanation for the increase in temperature.

We computed models of a photoionization precursor using the atomic rates and photoionization cross sections of Cox & Raymond (1985), much like the models that Ghavamian et al. (2000) applied to the photoionization precursor of Tycho's SNR. We used the Cox & Raymond shock code and specified the shock speed, pre-shock density and total swept-up column density to compute the radiation field impinging on the pre-shock plasma. Then we followed the time-dependent ionization states of the abundant elements, the photoionization heating and the radiative cooling to compute the temperature structure and the radiation in Hα and [N II]. At the relatively low temperatures encountered in the precursor, electron–ion equilibration by Coulomb collisions is rapid enough that we can assume $T_e = T_i$.

The models show that for shock speeds like those inferred from the Hα broad component widths and densities of the order of 1 cm^{-3}, the gas is heated and ionized over a length scale of the order of 0.5 pc, similar to the thickness of the observed diffuse emission. If the pre-shock neutral fraction is larger than about 0.3, the gas is heated to around 15,000 to 17,000 K. That can account for the 29 km s^{-1} Hα line width measured for the diffuse component, which corresponds to 18,000 K. This high temperature comes about because the He II λ304 line contributes strongly to the photoionization, and these 40.8 eV photons deposit considerable energy in the electrons. The temperature is determined by the balance between heating by photoionization and cooling by excitation of Lyα. At these temperatures, collisional excitation tends to dominate over recombination in generating the Hα line unless the neutral fraction is very small. In these models the order of magnitude increase in the Hα excitation rate, rather than an increase in the ionization state, is mostly responsible for the observed diffuse glow.

The photoionized and heated gas will also produce increased [N II] emission, since the excitation rate contains a Boltzmann factor exp(−22,000/T). The predicted [N II] emissivity increases by two or more orders of magnitude, depending on the initial temperature, and it can exceed 5% the Hα emissivity in the regions where the temperature is around 10,000 to 12,000 K. In general, however, the [N II]/Hα ratio for the diffuse region as a whole is predicted to be close to 1%, which lies below the observed values in both the ON and OFF spectra. The diffuse Hα line may contain some contribution from bulk motions along the line of sight, which would mean that the actual temperature is lower than 18,000 K and therefore the [N II]/Hα ratio is higher.

If the Hα emission line width of ∼29 km s^{-1} in the diffuse region is entirely thermal, it indicates a temperature of ∼18,000 K. The temperature depends on the pre-shock fraction of neutral hydrogen, but it is not likely to exceed ∼18,000 K, where excitation of hydrogen atoms to Lyα balances the heating. However, present and previous measurements of the narrow component line widths indicate temperatures of 28,000 K of more just before the gas encounters the shock front. Significant heating must occur between the positions of our diffuse spectra and the shock for the sharp increase from 18,000 to 28,000 K. We attribute the that final heating to a narrow precursor associated with cosmic-ray acceleration.

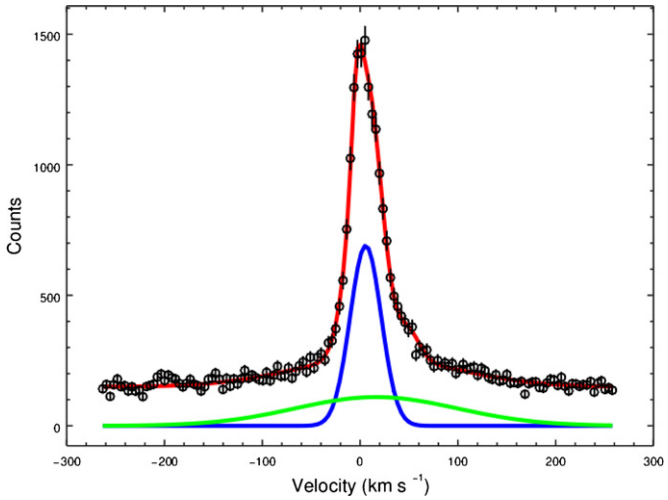

Figure 8. Model fit to the COS1 ON position (red), as well as separation of characteristic broad (green) and narrow (blue) components of the Balmer-dominated filament.

(A color version of this figure is available in the online journal.)

5.2. Hα Emission Lines in the Filament

We surveyed 12 positions along the Balmer-dominated filament. For each of the positions along the filament, we measured broad and narrow Hα emission line widths, centroids, broad component intensities, and broad to narrow intensity ratios I_b/I_n we report only those for the ON spectra since there was little variation between ON and OFF (see Table 4). We have assumed the broad and narrow line profiles to be Gaussian as shown in Figures 8–11. The fits to these particular spectra are of interest since Figure 8 shows the profile at the position corresponding to a UV spectrum obtained with COS on *HST* (Raymond et al. 2013), Figure 9 shows a clear offset between broad and narrow velocity centroids, and Figures 10 and 11 display the variation seen between ON and OFF spectra.

The width of the narrow component ranges from 35 to 43 km s^{-1} with little variation and no extreme outliers for all the positions measured in both the ON and OFF spectra. Variations in the ON and OFF spectra are due to slight fluctuations in intensity and slight spatial variation along the filament (see Figures 10 and 11). Our measurements compare nicely with the previous studies of the of Loop listed in Table 1 (Treffers 1981; Raymond et al. 1983; Hester et al. 1994). Treffers (1981) measured a narrow component line width of ∼35 km s^{-1} at a position that is further west than our chosen positions. Raymond et al. (1983) and Hester et al. (1994) reported widths of 31 ± 8 km s^{-1} and ∼33 km s^{-1}. These provide a good comparison for narrow component broadening since we have obtained higher resolution spectra. Our widths indicate a pre-shock gas temperature of ∼28,000 K, which is significantly higher than one would expect noting the ionization temperature of neutral hydrogen is 15,000 K. Pre-heating must be present in order to account for the broadening of the narrow component of Hα. As

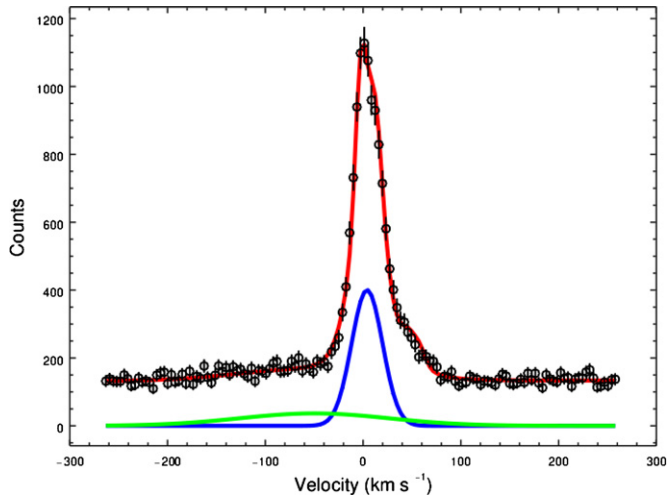

Figure 9. Model fit to the FUSEA OFF position (red), as well as separation of characteristic broad (green) and narrow (blue) components of the Balmer-dominated filament. Note the offset in the broad and narrow component centroids.

(A color version of this figure is available in the online journal.)

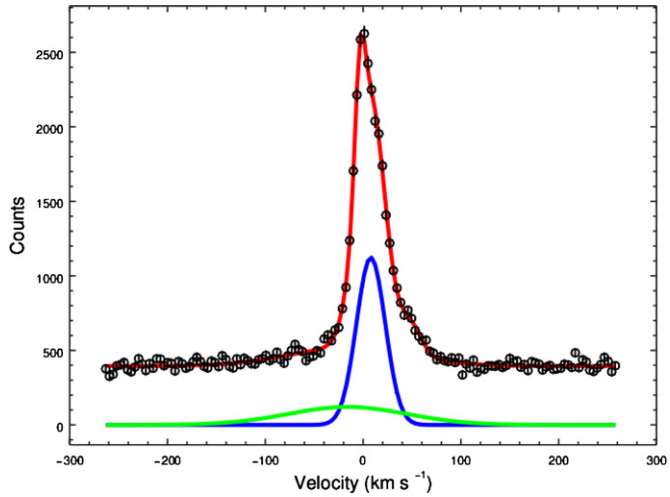

Figure 10. Model fit to the Nfil ON position (red), as well as separation of characteristic broad (green) and narrow (blue) components of the Balmer-dominated filament.

(A color version of this figure is available in the online journal.)

discussed in Section 3.2, photoionization by He I and He II can account for heating of the pre-shock gas up to ∼18,000 K. The rest of the heating must occur in a very thin precursor just before the gas encounters the shock front.

The line widths of the broad components range from ∼210 to ∼350 km s^{-1}, except for position S10, with a line width of 140 km s^{-1}. The small line width at S10 is similar to the values obtained by Raymond et al. (1983) and Hester et al. (1994) for a filament in that region. Because these slow shocks have begun the transition to the radiative phase (Long et al. 1992; Blair et al. 2005), we exclude S10 from further discussion. The line widths of the ON and OFF spectra are similar, except at S89, which has a broad component width of 347 ± 39 km s^{-1} in the ON and 213 ± 10 km s^{-1} in the OFF position. We attribute the discrepancy between ON and OFF line widths at this position to spatial variation across the filament. The bright filaments are tangencies of the rippled shock surface to the line of sight, and the ON and OFF spectra may sample different ripples (see Figures 10 and 11; Hester 1987).

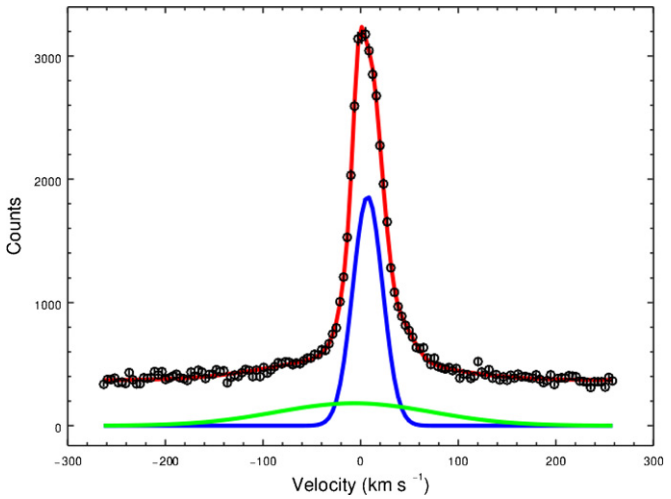

Figure 11. Model fit to the Nfil OFF position (red), as well as separation of characteristic broad (green) and narrow (blue) components of Balmer-dominated filament. Note the shift of the broad component centroid location between the ON and OFF Nfil fits.

(A color version of this figure is available in the online journal.)

Smith et al. (1991) noticed the a similar variation with aperture placement along the slit for observations of Tycho's SNR. On average, our measurements indicate broad component widths of ∼235 km s^{-1} for the OFF and ∼245 km s^{-1} for the ON positions. Except for Ghavamian et al. (2001), who measured a broad Hα line width of 262 ± 32 km s^{-1}, previous measured line widths have been smaller. The difference is likely due to the location of the measurements and the lower resolution spectra used in those studies. The line widths of the broad component represent the post-shock kinetic temperatures and shock velocities. For each position we computed temperatures and shock velocities using models with the assumption that $T_e = T_i$ by (Chevalier et al. 1980; see Table 5). The widths of the broad component indicate shock velocities of ∼400 km s^{-1} and proton temperatures $\sim 2.2 \times 10^6$ K, which are in agreement with Ghavamian et al. (2001). Our shock velocities, as well the one calculated by Ghavamian et al. (2001) are greater than those that have previously been measured. Higher shock velocities could be attributed to a lower density ISM in this region, as suggested by Kirshner & Taylor (1976) and Shull & Hippelein (1991).

Salvesen et al. (2009) measured proper motions for positions along the Cygnus Loop denoted by the letter (S). Table 5 compares our shock velocities determined from broad component line widths to their shock velocities determined from the product of proper motion and a 637 pc distance to the Cygnus Loop, based on the upper limit of Blair et al. (2009). Salvesen et al. (2009) calculated velocities ranging from 240–333 km s^{-1}, while ours average at ∼400 km s^{-1}, or a factor of ∼1.41 higher. Although many of our fiber positions on the filament were based on those of Salvesen, some of the inconsistency could be attributed to the slight variation in location on the filament as evidenced by our analysis of the ON and OFF spectra. The positions Salvesen observed could also be areas where greater rippling is occurring in the filament which is unrepresentative of the actual shock speed.

However, the fact that the distance to the Cygnus Loop is not well constrained, coupled with our velocities being greater by a factor of ∼1.41 suggests that the Cygnus Loop may be about 40% farther away than previously thought. This would make the distance to the remnant ∼890 pc. Salvesen et al.

Table 5
Shock Temperatures and Velocities

	Proper Motion (arcsec/39.1 yr)	v_{pm} (km s^{-1})	T_e (10^6 K)	v_{sON} (km s^{-1})	T_{sON} (10^6 K)	v_{sON}/v_{pm}	Distance (pc)
			Position				
S10	$3\farcs1 \pm 0\farcs2$	254	1.7	342 ± 46	1.6	1.35 ± 0.181	910 ± 126
$S89_{ON}$	$3\farcs7 \pm 0\farcs1$	294	1.9	457 ± 22	2.9	1.55 ± 0.075	1018 ± 56
$S89_{OFF}$	$3\farcs7 \pm 0\farcs1$	294	1.9	382 ± 6.0	2.1	1.30 ± 0.020	852 ± 27
S7	$3\farcs0 \pm 0\farcs1$	240	1.8	363 ± 5.0	1.8	1.51 ± 0.021	998 ± 35
S6	$4\farcs1 \pm 0\farcs2$	333	2.1	391 ± 3.0	2.1	1.17 ± 0.009	786 ± 39
S5	$3\farcs4 \pm 0\farcs2$	278	2.1	376 ± 4.0	1.9	1.35 ± 0.014	912 ± 55
S4	$2\farcs7 \pm 0\farcs2$	225	2.2	385 ± 7.0	2.0	1.71 ± 0.031	1176 ± 90
Fbk	...	...	...	425 ± 21	2.5	...	
EWfil	...	...	...	380 ± 4.0	2.0	...	
Nfil	...	...	...	429 ± 22	2.5	...	
COS 1	...	...	...	405 ± 8.0	2.5	...	
FUSEB	...	...	...	414 ± 5.0	2.4	...	
FUSEA	...	...	...	428 ± 7.0	2.6	...	

Notes. Shock velocities and temperatures computed from measured broad component Hα line widths for ON and OFF positions. The proper motions of several fiber positions listed from Salvesen et al. (2009) (denoted by S) and shock velocities v_{pm}, were calculated from the product of the proper motion and distance (637 pc) to the Cygnus Loop (Blair et al. 2009). Also listed are the electron temperatures determined using an X-ray spectral APEC model. See Salvesen et al. (2009). The ratio v_s/v_{pm} shown allows comparison of our measurements for shock velocities with those of Salvesen.

(2009) also measured post-shock electron temperatures using X-ray data from *ROSAT*, providing further comparison for our temperature equilibrium analysis. Our shock speeds indicate a post-shock temperature $\sim 2.2 \times 10^6$ K while those of Salvesen indicate a slightly lower post shock temperature $\sim 1.2 \times 10^6$ K. However, the X-ray temperatures are uncertain. More recent data are poorly fit by single-temperature models (Tsunemi et al. 2007), and two-temperature models include components around $\sim 4.6 \times 10^6$ K that would require 600 km s^{-1} shocks if the emission is thermal (Katsuda et al. 2008).

Broad-to-narrow intensity ratios were also obtained. The ratios are ~0.9 for both the ON and OFF spectra. S10 (0.340 ± 0.31 and 0.595 ± 0.15) and Fbk (0.597 ± 0.112 and 0.428 ± 0.079) gave lower ratios for ON and OFF, respectively. The very low I_b/I_n in these two southern locations may mean that the diffuse emission is different there, as might be expected for a precursor photoionized by radiative rather than non-radiative shocks. Broad-to-narrow intensity ratios are sensitive to the diffuse Hα component since it contributes to the narrow line intensity. S4 gave the greatest intensity ratios in both the ON and OFF positions, 1.39 ± 0.15 and 1.18 ± 0.03. S4 is located near the middle of the filament. The ratios tend to decrease as you travel north or south along the filament. This may be due to the additional intensity contributions from the diffuse emission at the various positions. The uncertainties for I_b/I_n quoted in Table 4 do not include the uncertainty due to spatial variations in the diffuse emission. As a rough estimate, the diffuse Hα intensity is up to ~20% of that of the narrow component intensity, implying about a ~10% uncertainty in I_b/I_n.

The intensity ratio is sensitive to both shock velocity and electron–ion temperature equilibrium. From the equilibration models presented in (Ghavamian et al. 2001; their Figure 10) it is evident that our average value of ~0.9 is slightly below the lowest value they modeled even for full equilibration. This indicates that T_e/T_i is generally within the range of 0.7–1.1, suggesting effective equilibrium. It is important to note that the van Adelsberg et al. (2008) models could not provide a match based on the line width provided by Ghavamian et al. (2001) of 262 km s^{-1} and I_b/I_n 0.59. The discrepancy between the van Adelsberg models and the Ghavamian measurements may be due to contamination of the narrow component by emission from the precursor (Nikolić et al. 2013).

6. DISCUSSION

The NE non-radiative filament in the Cygnus Loop has allowed us to better quantify T_e/T_i as well as determine shock properties of the including pre-heating, velocities, and temperatures.

The optical echelle observations of the northeast filament of the Cygnus Loop constrain pre-heating mechanisms of Balmer-dominated filaments produced by non-radiative collisionless shocks in the SNR. After accounting for instrumental broadening, the faint diffuse emission region extending ahead of the main filament has an Hα line width that is greater than expected, 29 km s^{-1}, and it also shows faint [N II] emission. The line profile width indicates a temperature ~18,000 K. Photoionization heating in this region accounts for the ~18,000 K temperature, but not the ~28,000 K temperature from the narrow component of the filament spectra. We attribute the additional heating to a thin cosmic-ray precursor just ahead of the shock front (see Figure 12).

Our measurements of $I_b/I_n \sim 0.9$ confirm effective electron–ion equilibrium in the post-shock region suggested by Ghavamian et al. (2001). However, emission from the narrow cosmic-ray precursor described above may contribute to the narrow component intensities at the filament and artificially lower I_b/I_n, perhaps producing the variation in the ratio among different locations. This contribution may explain the discrepancy between the van Adelsberg models and the observations of Ghavamian et al. (2001) and Nikolić et al. (2013).

From the broad component of the Hα line widths, we estimate shock speeds of ~400 km s^{-1}. Our speeds are ~1.41 times larger than those that Salvesen et al. (2009) computed using proper motions and the upper limit of the distance given by Blair et al. (2009) of 637 pc. The distance to the Cygnus Loop provides the greatest uncertainty for Salvesen's velocity calculations.

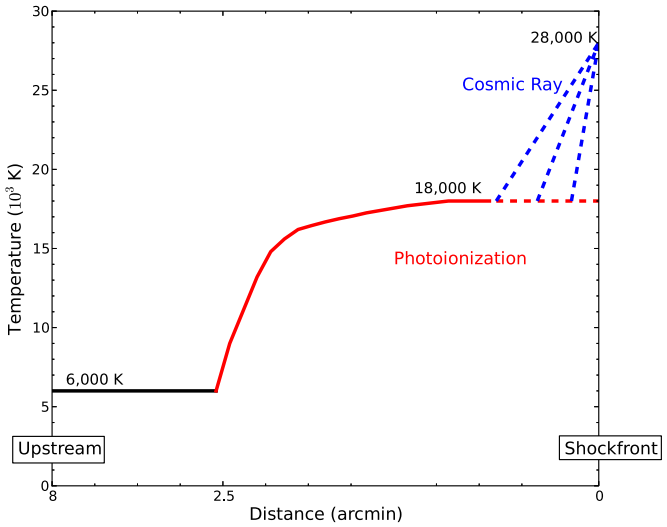

Figure 12. Schematic diagram of the two precursors—a thick photoionization precursor (red) that heats the ISM gas to 18,000 K and a thin cosmic-ray precursor (blue) that heats it to 28,000 K.

(A color version of this figure is available in the online journal.)

Previous attempts to constrain the distance have been made, but they vary widely from 440 to 1400 pc (Minkowski 1958; Sakhibov & Smirnov 1983; Shull & Hippelein 1991; Blair et al. 1999, 2005, 2009). Blair et al. (2009) provided the most robust upper limit to the distance by detecting O VI absorption in the spectrum of a subdwarf OB (sdOB) background star. However the luminosity of the star can only be estimated, and determining distances to sdOB stars is difficult. Blair et al. (2005) determined a distance to the Cygnus Loop using proper motion measurements with a position near our fiber FBK. They found a distance of 540 ± 90 pc and a shock velocity ∼180 km s^{-1}. Unfortunately, our fiber position is further south than the position used in their study (Blair et al. 2005) and offset behind the brightest part of the filament. We apparently observed an undecelerated area of the shock, while Blair et al. (2005) observed a region where the shock encounters a dense cloud. That accounts for the large difference in shock velocity and hence distance between our analysis and that of Blair et al. (2005). Our velocities imply the distance to the Cygnus Loop is ∼1.41 times greater than previously thought, implying a new distance ∼890 pc. It is important to note our computation of shock speeds assumes $T_e = T_i$. Based on our values of I_b/I_n, this is a proper assumption. However if the equilibrium value were at the lower end of the allowed range given by the Ghavamian et al. (2001) models, $T_e = 0.7\,T_i$, then our inferred shock speeds would be 10% smaller. Lower shock speeds provide a lower limit to our inferred distance to the Cygnus Loop of ∼800 pc, which is still 25% larger than that of Blair et al. (2009).

Salvesen et al. (2009) measured electron X-ray temperatures, which we can compare to our proton temperatures. Our values of $\sim 2.2 \times 10^6$ K are in reasonable agreement with the X-ray temperatures in the region where the majority of our fibers are located. Lower temperatures and shock speeds were obtained at positions farther south starting at S10. The low resolution X-ray data used by Salvesen et al. (2009) are poorly fit by single temperature models, so they provide only a rough temperature. Nevertheless, $T_e \sim T_i$ is suggested by the comparison.

Finally, we consider the implications of our observations for cosmic-ray acceleration discussed in Section 3.1. *Fermi*-LAT observations show that the Cygnus Loop produces gamma rays, probably by pion decay following hadronic interactions, but that the energy in the cosmic-rays is only ∼0.1% of the SN energy (Katigiri et al. 2011). Much of the acceleration may have occurred earlier in the SNR evolution when the shock speeds were higher, but in any case, the shocks we observe are unlikely to accelerate cosmic rays very efficiently. If they did, the energy lost to cosmic rays would imply that a higher shock speed, and therefore an even larger distance to the Cygnus Loop, would be needed to account for the observed shock temperatures. If more than 10% of the energy dissipated in the shock went into cosmic rays, the distance estimates would increase by more than 20%, which would be very difficult to reconcile with the distance estimates of Blair et al. (2009).

The heating indicated by the narrow component line widths seems to require some cosmic-ray acceleration, and it can used to constrain the diffusion coefficient in the cosmic-ray precursor (Hester et al. 1994). We find that photoionization produces substantial pre-shock heating, but that further heating from ∼18,000 K to ∼28,000 K must occur between the positions of our diffuse spectra and the filament spectra. That separation of about 1.5×10^{18} cm is an upper limit to the cosmic ray precursor thickness, and $d \sim \kappa/v_s$, so that the diffusion coefficient, $\kappa < 6 \times 10^{25}$ cm^2 s^{-1}. This is an order of magnitude smaller than the value estimated by Li & Chen (2012) from the *Fermi* observations, but their estimate would characterize diffusion throughout the history of the remnant, and it would pertain to very energetic particles.

7. CONCLUSION

Constraining pre-shock heating mechanisms and electron–proton equilibrium in SNRs is integral for understanding non-radiative collisionless shocks in astrophysical environments. Faint Balmer emission in the northeast limb of the Cygnus Loop has provided a mechanism for improving this understanding. Our analysis of 12 positions spanning the Loop along with diffuse Hα emission ahead of the filament has allowed us to conclude that (1) Narrow component broadening is due to a photoionization precursor heating the pre-shock gas up to 18,000 K in addition to a thin cosmic-ray precursor that heats the gas just before it encounters the shock-front to 28,000 K. (2) Effective electron–ion temperature equilibration in the shock leads to $T_e \sim T_i$. (3) Our measurements imply that the distance to the Cygnus Loop is greater than previously thought by about 40%, giving a new distance estimate of ∼890 pc. (4) Cosmic-ray acceleration in the Cygnus Loop is not efficient at this point in its evolution, but the diffusion coefficient has been constrained to $\kappa < 6 \times 10^{25}$ cm^2 s^{-1}.

This work is supported by the National Science Foundation REU and Department of Defense ASSURE programs under NSF Grant no. 1262851 and by the Smithsonian Institution. This work was partially supported by the grant HST-60-12885 to the Smithsonian Institution.

We acknowledge S. Tokarz for data reduction. We would also like to acknowledge use of the MMT.

Facility: MMT: Hectochelle

REFERENCES

Allen, G. E., Houck, J. C., & Sturner, S. J. 2008, ApJ, 683, 773
Ballet, J., Arnaud, M., & Rothenflug, R. 1984, A&A, 133, 357
Blair, W. P., Sankrit, R., & Raymond, J. C. 2005, AJ, 129, 2268
Blair, W. P., Sankrit, R., Raymond, J. C., & Long, K. S. 1999, AJ, 118, 942

Blair, W. P., Sankrit, R., Torres, S. I., Chayer, P., & Danforth, C. W. 2009, ApJ, 692, 335
Blandford, R., & Eichler, D. 1987, PhR, 154, 1
Boulares, A., & Cox, D. P. 1988, ApJ, 333, 198
Chevalier, R. A., & Gardner, J. 1974, ApJ, 192, 457
Chevalier, R. A., Kirshner, R. P., & Raymond, J. C. 1980, ApJ, 235, 186
Chevalier, R. A., & Raymond, J. C. 1978, ApJL, 225, L2
Cox, D. P., & Raymond, J. C. 1985, ApJ, 298, 651
Curiel, S. 1992, PhD thesis Univ. Nacional Autònoma de Mèxico
Doe, S., Nguyen, D., Stawarz, C., et al. 2007, in ASP Conf. Ser. 376, Astronomical Data Analysis Software and Systems XVI, ed. R. A. Shaw, F. Hill, & D. J. Bell (San Francisco, CA: ASP), 543
Dopita, M. A., & Sutherland, R. S. 1996, ApJS, 102, 161
Draine, B. T. 1980, ApJ, 241, 1021
Fesen, R. A., Blair, W. P., & Kirshner, R. P. 1982, ApJ, 262, 171
Freeman, P., Doe, S., & Siemiginowska, A. 2001, Proc. SPIE, 4477, 76
Fruscione, A., McDowell, J. C., Allen, G. E., et al. 2006, Proc. SPIE, 6270, 62701V
Ghavamian, P., Raymond, J. C., Hartigan, P., & Blair, W. P. 2000, ApJ, 535, 266
Ghavamian, P., Raymond, J. C., Smith, R. C., & Hartigan, P. 2001, ApJ, 547, 995
Ghavamian, P., Winkler, P. F., Raymond, J. C., & Long, K. S. 2002, ApJ, 572, 888
Graham, J. R., Wright, G. S., Hester, J. J., & Longmore, A. J. 1991, AJ, 101, 175
Haffner, L. M., Reynolds, R. J., Tufte, S. L., et al. 2003, ApJS, 149, 405
Heng, K. 2010, PASA, 27, 23
Hester, J. J. 1987, ApJ, 314, 187
Hester, J. J., Raymond, J. C., & Blair, W. P. 1994, ApJ, 420, 721
Katigiri, H., Tibaldo, L., Ballet, J., et al. 2011, ApJ, 741, 44
Katsuda, S., Tsunemi, H., Kimura, M., & Mori, K. 2008, ApJ, 680, 1198
Kirshner, R. P., & Taylor, K. 1976, ApJL, 208, L83
Lee, J.-J., Koo, B.-C., Raymond, J., et al. 2007, ApJL, 659, L133
Lee, J.-J., Raymond, J. C., Park, S., et al. 2010, ApJL, 715, L146
Levenson, N. A., Graham, J. R., Aschenbach, B., et al. 1997, ApJ, 484, 304
Levenson, N. A., Graham, J. R., Keller, L. D., & Richter, M. J. 1998, ApJS, 118, 541
Li, H., & Chen, Y. 2012, MNRAS, 421, 935
Long, K. S., Blair, W. P., Vancura, O., et al. 1992, ApJ, 400, 214
McKee, C. F., & Hollenbach, D. J. 1980, ARA&A, 18, 219
Minkowski, R. 1958, RvMP, 30, 1048
Morlino, G., Bandiera, R., Blasi, P., & Amato, E. 2012, ApJ, 760, 137
Mullan, D. J. 1971, MNRAS, 153, 145
Nikolić, S., van de Ven, G., Heng, K., et al. 2013, Sci, 340, 45
Ohira, Y. 2012, ApJ, 758, 97
Raymond, J. C. 1991, PASP, 103, 781
Raymond, J. C., Blair, W. P., Fesen, R. A., & Gull, T. R. 1983, ApJ, 275, 636
Raymond, J. C., Davis, M., Gull, T. R., & Parker, R. A. R. 1980, ApJL, 238, L21
Raymond, J. C., Ghavamian, P., Sankrit, R., Blair, W. P., & Curiel, S. 2003, ApJ, 584, 770
Raymond, J. C., Ghavamian, P., Willaims, B. J., et al. 2013, ApJ, 778, 161
Raymond, J. C., Vink, J., Helder, E. A., & de Laat, A. 2011, ApJL, 731, L14
Reynolds, S. P., & Ellison, D. C. 1992, ApJL, 399, L75
Sakhibov, F. K., & Smirnov, M. A. 1983, SvA, 27, 395
Salvesen, G., Raymond, J. C., & Edgar, R. E. 2009, ApJ, 702, 327
Sankrit, R., & Blair, W. P. 2002, ApJ, 565, 297
Sankrit, R., Blair, W. P., Raymond, J. C., & Long, K. S. 2000, BAAS, 31, 1434
Shull, J. M., & McKee, C. F. 1979, ApJ, 227, 131
Shull, P., Jr., & Hippelein, H. 1991, ApJ, 383, 714
Smith, R. C., Kirshner, R. P., Blair, W. P., & Winkler, P. F. 1991, ApJ, 375, 652
Smith, R. C., Raymond, J. C., & Laming, J. M. 1994, ApJ, 420, 286
Sollerman, J., Ghavamian, P., Lundqvist, P., & Smith, R. C. 2003, A&A, 407, 249
Szentgyorgyi, A., Furesz, G., Cheimets, P., et al. 2011, PASP, 123, 1188
Szentgyorgyi, A. H., Raymond, J. C., Hester, J. J., & Curiel, S. 2000, ApJ, 529, 279
Treffers, R. R. 1981, ApJ, 250, 213
Tsunemi, H., Katsuda, S., Nemes, N., & Miller, E. D. 2007, ApJ, 671, 1717
van Adelsberg, M., Heng, K., McCray, R., & Raymond, J. C. 2008, ApJ, 689, 1089
Vink, J., Bleeker, J., van der Heyden, K., et al. 2006, ApJL, 648, L33
Zel'dovich, Ya. B., & Raizer, Yu. P. 1966, Physics of Shock Waves and High Temperature Phenomena (New York: Academic Press)